View metadata, citation and similar papers at core.ac.uk

brought to you by CORE

provided by Earth-prints Repository

Accepted Manuscript

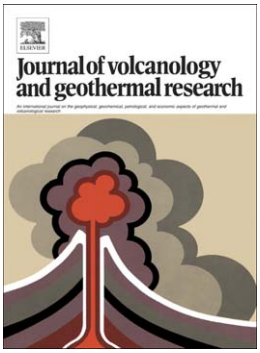

Uncertainties in lava flow hazard maps derived from numerical simulations: The case study of Mount Etna

Simone Tarquini, Massimiliano Favalli

PII: S0377-0273(13)00136-4
DOI: doi: 10.1016/j.jvolgeores.2013.04.017
Reference: VOLGEO 5138

To appear in: *Journal of Volcanology and Geothermal Research*

Received date: 29 January 2013
Accepted date: 27 April 2013

Please cite this article as: Tarquini, Simone, Favalli, Massimiliano, Uncertainties in lava flow hazard maps derived from numerical simulations: The case study of Mount Etna, *Journal of Volcanology and Geothermal Research* (2013), doi: 10.1016/j.jvolgeores.2013.04.017

This is a PDF file of an unedited manuscript that has been accepted for publication. As a service to our customers we are providing this early version of the manuscript. The manuscript will undergo copyediting, typesetting, and review of the resulting proof before it is published in its final form. Please note that during the production process errors may be discovered which could affect the content, and all legal disclaimers that apply to the journal pertain.

ACCEPTED MANUSCRIPT

Uncertainties in lava flow hazard maps derived from numerical simulations: the case study of Mount Etna

Simone Tarquini* and Massimiliano Favalli
Istituto Nazionale di Geofisica e Vulcanologia, Sezione di Pisa, Italy

Abstract

The procedure for the derivation of a hazard map for lava flows at Mount Etna through lava flow simulations is critically reviewed. The DOWNFLOW code is then used to explore the sensitivity of the hazard map with respect to input settings. Three parameters are varied within ranges close to values recently applied to derive similar hazard maps: (i) the spacing between computational vents; (ii) the spatial probability density function (PDF) for future vent opening; and (iii) the expected length of future lava flows. The effect of increasing the spacing between computational vents tends to be compensated at the lower elevations, and a vent spacing smaller than about 500 m warrants an overall difference with respect to a reference map which is smaller than 6-8%. A random subsampling of the elements used to obtain the input vent opening PDF (-20%, -40% and- 60%) originates significant but drastically smaller differences in the obtained map with respect to the reference one (~10%, ~12.5% and ~17% respectively, on average). In contrast, our results show that changes in the expected flow length originate, by far, the highest changes in the obtained hazard map, with overall differences ranging between ~20% and ~65%, and between ~30% and ~95% if computed only over inhabited areas. The simulations collected are further processed to derive maps of the confluence/diffluence index, which quantifies the error introduced, locally, when the position of the vent is misplaced by a given distance.

1. Introduction

* Simone Tarquini, Istituto Nazionale di Geofisica e Vulcanologia, Sezione di Pisa, Via della Faggiola 32, 56100 Pisa, Italy (tarquini@pi.ingv.it)

ACCEPTED MANUSCRIPT

Compared to other paroxysms occurring at volcanoes, lava flows are one of the less dangerous phenomena (Pyle, 1995; Simkin et al., 2001). Nevertheless, on the many populated basaltic volcanoes on Earth, the effects of effusive eruptions need to be adequately assessed for a proper land use planning and for civil defence purposes during ongoing events (Barberi et al., 1993; Wadge et al., 1994; Kauahikaua et al., 1995; Favalli et al., 2006, 2009a, 2012; Kelman and Mather, 2008; Chirico et al., 2009; Vicari et al., 2011a). This is especially true at Mount Etna (Italy), where several times in the last centuries inhabited areas have been inundated by lava flows, including the town of Catania in 1669 (Crisci et al., 2003 and references therein).

In recent years, a number of authors applied different lava flow simulation codes to derive hazard maps at Mount Etna: SCIARA (e.g. Crisci et al., 2008), DOWNFLOW (e.g. Favalli et al., 2009a, Figure 1), and MAGFLOW (e.g. Cappello et al., 2011a). In all these cases, the use of increasingly powerful computational resources and/or the application of probabilistic methods allow the collection, and the subsequent processing, of a large number of simulations, and the output of this processing is represented by a map where each point is attributed with the probability of being inundated by a future lava flow.

The evidence is that, although rather different simulation codes are used, the procedures applied to obtain hazard maps are fairly equivalent. This convergence should not be surprising, because all the three mentioned codes, each one within its own assumptions, proved to be valid tools for lava flow simulations, and are then expected to produce similar outputs, which are processed in a similar way to obtain the same target (the hazard map).

Nevertheless, beyond the procedural similarities, input settings have been quite different in different cases. Diversity in settings includes different characteristics for the simulated events and different spatial arrangement of the database of simulations. To give the end-user of these maps an estimate of the uncertainties involved, it is important to assess to what extent changes in input settings are reflected in the final maps, weighting the impact of single parameters.

ACCEPTED MANUSCRIPT

In the following we will address this point, quantifying the discrepancies between different hazard maps obtained by varying input settings within ranges close to previously applied values. The test site is Mount Etna, and we take as reference the map presented by Favalli et al. (2009a).

2. Methods

2.1. Lava flow simulation codes

Numerical codes for the simulation of lava flows can be classified in deterministic or probabilistic (i.e. Costa and Macedonio, 2005a). Deterministic models implement some simplification of the physical governing equations of lava flows. Many of them are based on the cellular automata paradigm (Barca et al., 2004; Miyamoto and Sasaki, 1997; Crisci et al., 2004; Del Negro et al., 2005; Hidaka et al., 2005; Proietti et al., 2009), but different computational solutions have been proposed (e.g. Costa and Macedonio, 2005b; Herault et al., 2011). Probabilistic models, instead, determine the spreading of lavas over the topography through some perturbation of the steepest descent path calculated from the vent (Macedonio et al., 1990; Felpeto et al., 2001; Favalli et al., 2005). Overall, deterministic models are more demanding in terms of computational resources by several orders of magnitude with respect to probabilistic models. This implies that while probabilistic codes can be readily used on a general purpose personal computer, deterministic codes might require specific computational facilities such as CPU clusters designed for parallel computing (e.g. Rongo et al., 2011) or dedicated graphic processor units (Bilotta et al., 2011). A further substantial difference is that deterministic codes need a long list of input physical parameters describing the lava supplied at each computational step, while probabilistic codes are much less demanding in terms of input requirements (Renshler, 2005; Tarquini and Favalli, 2011).

ACCEPTED MANUSCRIPT

2.2. The DOWNFLOW code

In the present work, we use the probabilistic code DOWNFLOW (Favalli et al., 2005) which has been often used at Mount Etna (e.g. Tarquini and Favalli 2011; Favalli et al., 2011) and other volcanoes (Favalli et al., 2009c, 2012). DOWNFLOW approaches lava flows as relatively slow gravity-driven mass movements over the Earth surface. A lava flow moves approximately along the steepest descent path (SDP) defined by the pre-emplacement morphology, but it can surmount obstacles and spread over the topography or bifurcate in multiple directions. DOWNFLOW accounts for these complexities by tracing a number N of SDPs, each SDP being calculated over a topography whose elevation is perturbed at each point, randomly, by a value varying within a given range $\pm\Delta h$. N and Δh are the two parameters that can be tuned to calibrate the code to different scenarios (e.g. different characteristics of lava flows at different volcanoes, Favalli et al., 2006, 2011, 2012); the cumulative area covered by the N paths provides the area susceptible of being inundated. The result of a simulation is represented by a map where each pixel records the number of times n that it has been reached by a lava path (Figure 2a). DOWNFLOW neither provides any insight about the flow velocity nor is able to determine, by itself, the flow length. The code is able to fill and overcome depressions (see Favalli et al., 2009c), so that the SDPs are not stopped by DEM irregularities or by occasional barriers, and paths continue beyond the morphological obstacles. Therefore, the SDPs always reach the boundary of the computational domain and the maximum runout distance constitutes an additional constraint. This constraint is added by taking simply into consideration the length of past eruptions. For Mount Etna, the analysis of a large number of known lava flows suggests a negative correlation between the maximum length of lava flows and the elevation of the vent (Guest, 1982). Favalli et al. (2009a, 2009d) expresses this correlation using two probabilistic functions relating lava flow length with the elevation of the vent at Mount Etna (Figure 2b, 2c). A negative correlation between the maximum length of lava flows

ACCEPTED MANUSCRIPT

and the elevation of the vent has been found to hold also at other basaltic volcanoes such as Nyiragongo and Mount Cameroon (Favalli et al., 2009c, 2012).

2.3. From numerical simulations to quantitative hazard maps of lava flows

Three lava flow simulation codes have been recently applied to obtain lava flow hazard maps at Mount Etna: SCIARA (e.g. Rongo et al. 2011), DOWNFLOW (e.g. Favalli et al. 2009a) and MAGFLOW (Cappello et al., 2011b) for a cumulative 9 papers published between 2008 and 2011 (Table 1). In all these applications, a series of fundamental elements are necessary in addition to the lava flow simulation code: (i) a digital model of the volcano topography; (ii) the choice of the computational vents (iii) a probability density function (PDF) for future vent opening on the volcano (which is the probability of activation of each computational vent); (iv) a function/map providing the characteristics of the expected effusions at each computational vent (e.g. effusion rate and duration). For the production of a risk map, we also need the distribution of the exposed value and the associated vulnerability (e.g. Favalli et al., 2009a).

The time factor in hazard calculations is a critical aspect. It is generally assumed that the temporal process generating the eruptive events is an inhomogeneous Poisson process (Salvi et al., 2006; Smethurst et al., 2009), i.e. a Poisson process with an intensity of occurrence in time which is not constant. In particular, for Mount Etna the intensity of flank eruption times appears to be rather variable with a strong rise from the mid-1900s (e.g. Smethurst et al., 2009) from intensity values ~0.15 $years^{-1}$ up to values ~0.5 $years^{-1}$ at the present days (corresponding to recurrence times ~2 years). Thus, for example, a choice of 50 years (see for example Cappello et al., 2011a) as the time window for the computation of a lava flow hazard map can be tricky. In addition, upon the emplacement of a new lava flow, the original topography no longer represents a reliable reference for simulating future lava flows in the same area (Tarquini and Favalli, 2010). This is the reason for a tendency in producing maps giving, point by point, the probability of lava inundation for the next

ACCEPTED MANUSCRIPT

eruption (i.e. lava flow invasion susceptibility maps, e.g Crisci et., 2010; Favalli et al. 2009a) rather than maps giving probability of inundation in a given time interval (hazard maps in a more proper sense). In any case, as we will discuss below, it is straightforward to add a time frame to a lava flow invasion susceptibility map to get a time-constrained hazard map, at least under some simplifying assumptions.

Explaining formula (2) in Favalli et al. (2009d) the probability H_i that a generic cell i of the computational domain (the DEM used for the simulations) is invaded by a lava flow in the case of a future eruption is given by

$$H_i = \sum_j \rho_{Vj} \Delta x \Delta y \cdot P_{ij} \cdot P_{Lij} \tag{1}$$

where the summation j is over all the computational vents, ρ_{Vj} is the average value in the cell j of the spatial PDF for future vent opening, Δx and Δy are the dimensions of the computational cells (hence the probability $p^{(j)}$ of a vent activation inside the area of the j^{th} cell is $\rho_{Vj}\Delta x\Delta y$), P_{ij} takes the value of 1 or 0 according to whether the pixel i is or is not, respectively, inundated by a lava flow originating from pixel j (irrespective of the distance between i and j), and P_{Lij} is the probability that a lava flow originating from j is long enough to reach i along the calculated flow path.

Rongo et al. (2011) compiled lava flow invasion susceptibility maps at Mount Etna applying the code SCIARA. They considered at each computational vent the possibility of occurrence of 6 different types (identified by and index e) of events, according to given classes of total erupted volume, duration and effusion rate pattern. Rongo et al. (2011) give the following definition of the lava flow invasion susceptibility at any generic cell of coordinates x,y of the computational domain:

$$H_{x,y} = \sum_{i=1}^{n_{x,y}} p_e^{(i)} \tag{2}$$

ACCEPTED MANUSCRIPT

which is the sum of the probabilities $p_e^{(i)}$ of occurrence of the number $n_{x,y}$ of events which reach the cell i; $n_{x,y}$ is a subset of the total SCIARA simulations carried out, while the probability $p_e^{(i)}$ accounts for both the probability of bare activation of the vent and for the probability of occurrence of the given kind of event e from that vent.

The formula used with MAGFLOW (Cappello et al., 2011a) is:

$$Hazard(x, y, \Delta t) = \sum_{i=1}^{N} \sum_{e=1}^{6} p_a(v_i) \cdot p_e(v_i) \quad (3)$$

The hazard at the point x, y is given by the double summation over the probabilities of activation of each computational vent (v_i, Σ_i) and over the probability of occurrence of the given event type (v_i, Σ_e, with e varying between 1 and 6 because these authors considered the same spectrum of 6 kinds of possible events used by Rongo et al., 2011). All with the premise that the summation is restricted to the $\boldsymbol{N}$ events reaching point x, y.

H_i, $h_{x,y}$ and $Hazard(x,y,\Delta t)$ of equations (1) to (3) uses different notations, but all of them express the probability of inundation by a future lava flow at a given point, which is identified by the ordinal subscript i in (1), or by the spatial coordinates x and y of the i^{th} cell in (2) and (3). The only substantial difference is that in (3) a given time window Δt is considered through its presence in the vent activation probability $p_a(v_i)$. Several notation differences express an equivalent concept. As an example, the boolean parameter P_{ij} which appear in (1) is not contained in (2) and (3) because it is just assumed in the premises, i.e. the sum is restricted to events that reach/cover point i/x,y. Another example is the probability of activation of each vent that is expressed in (1) by the multiplication of the probability density function by the cell area ($\rho_{Vj}\Delta x\Delta y$), in (3) is expressed by the single term p_a, and in (2) is embedded in the probability of occurrence of single events p_e.

In addition to the mentioned time constraint in (3), the probability of occurrence of different kinds of events at different vents is a major difference between the three formulas: in (1) the variety of events is accounted for by assigning different probabilities of attaining different flow lengths (P_{Lij}, Figure 2b-c); in (2) the relative probabilities of 6 different classes of events are assumed

ACCEPTED MANUSCRIPT

constant throughout all the computational vents; while in (3) the relative probabilities of occurrence of 6 different classes of events (p_e) vary at each point according to a function which accounts for the actual events recorded in the past 400 years.

In Favalli et al. (2009a; 2009d), it is shown how to convert lava flow invasion susceptibility maps (e.g. eq. 1 and 2) into maps with probabilities of occurrence in a time window under the assumption that eruptions follow a Poisson distribution in time.

Given the spatial PDF for future vent opening $\rho_V(x,y)$, the probability $p^{(j)}$ that next eruption occurs in the cell j is $\rho_{Vj}\Delta x\Delta y$ where ρ_{Vj} is, again, the average value in the cell j. On the other hand, under the hypothesis of having a Poisson process in time, the probability of having at least an eruption in a given time Δt inside the cell j is (Favalli et al., 2009a):

$$p_{erupt}(x,y,\Delta t) = 1 - e^{-(\Delta t/T)\rho_V(x,y)\Delta x\Delta y} \cong (\Delta t/T)\,\rho_V(x,y)\Delta x\Delta y \tag{4}$$

where T is the average recurrence interval between eruptions and the last equality holds when the expression $(\Delta t/T)\ \rho_{Vj}\Delta x\Delta y$ is much smaller than unity. For time frames ≤10 yr, for example, this expression is always less than 10^{-6} in the case of Mount Etna. Turning the probability of the left hand side of equation 4 into a spatial PDF we obtain:

$$\rho(x,y,\Delta t) \cong (\Delta t/T)\,\rho_V(x,y) \tag{5}$$

If we want to calculate a time constrained hazard map using DOWNFLOW we simply have to substitute the spatial PDF for future vent opening ρ_{Vj} in equation 1 with the spatial PDF of having at least one eruption in a given time frame Δt (i.e. equation 5) obtaining:

$$\tilde{H}_i = (\Delta t/T)\sum_j \rho_{Vj}\Delta x\Delta y \cdot P_{ij} \cdot P_{Lij} \tag{6}$$

where the $\tilde{H}_i$ is now a proper hazard expressing the probability for the cell i to be invaded by lava flows in the time interval Δt. Of course we are, again, supposing that the recurrence time T has negligible variations in the time frame Δt considered and that in the time interval Δt we have a

ACCEPTED MANUSCRIPT

negligible probability of having two overlapping lava flows, so that the input topography is a reliable reference for the future eruptions we are trying to simulate.

Comparison between equations 1 and 6 shows that computing probabilities of inundation for the next eruption is equivalent to computing probabilities of inundation in a time interval equal to the recurrence time T (so that the factor $\Delta t/T$ in equation 6 is unity, obtaining equation 1). This is the reason we refer to the output of equation 1 as hazard map, either considering it a proper hazard map with a time interval of a recurrence time or keeping in mind that to convert it to a proper hazard map with a time horizon of Δt simply requires a multiplication by $\Delta t/T$.

Cappello et al. (2011a, 2011b) express the temporal term as $1 - e^{-\lambda(t)\Delta t}$, which can be approximated to 1 for the current value of the intensity function of occurrence in time $\lambda(t) \sim 1/2$ (Smethurst et al., 2009) and the considered time interval $\Delta t = 50$ years. The same authors express the probability of activation at a given point as $p_a(x,y,\Delta t) = (1 - e^{-\lambda(xy)\Delta x\Delta y})\,(1 - e^{-\lambda(t)\Delta t})$, where $\lambda(xy)$ is the spatial recurrence rate, and where the temporal term do not alter the hazard value. But this is not true, because the temporal term is not negligible (e.g. see Favalli et al., 2009d).

In the section 3.2 we will explore the modifications to the hazard map due to changes in: (a) the number of and the spacing between the computational vents; (b) the probability of activation of single vents; (c) the characteristics of the expected events at single vents.

2.4. The expected impact upon given vent opening

By combining a hazard map with a map of the exposed value together with the relative vulnerability, a risk map can be derived straightforwardly (e.g. Favalli et al., 2009a; 2012). Nevertheless, further applications are possible beside the relatively obvious standard risk map. As an example, the availability of simulation databases can be readily used for the analysis of the expected impact on an exposed value from given vents. In the case of Mount Etna, the first

ACCEPTED MANUSCRIPT

applications in this sense has been published by Favalli et al. (2009d). These authors selected five target-villages on the volcano flanks, and highlighted the areas of the volcano where a vent opening would originate a flow which will impact the villages. Similarly, Crisci et al. (2010) and Rongo et al. (2011), by applying a query on the simulation database, highlighted the computational vents whose simulations cover a given target, hence revealing the areas which threaten the same target upon vent opening. A similar example is presented by Vicari et al. (2011b).

Favalli et al. (2009a) combined the hazard map of Figure 1 with a database of buildings (170,156 separated elements) to obtain a "standard" risk map for buildings. In addition to this, the same authors presented a "map of the reversed risk", where each computational vent is assigned with the value of the expected impact on buildings upon vent activation (expressed, in a probabilistic way, in m^2 of impacted buildings).

It is apparent that, when the focus is on the vents, the spacing of the mesh of computational vents establishes the resolution of the resulting analysis.

2.5. The confluence/diffluence index

Further uses of the same databases of simulations have been proposed. Crisci et al. (2010) suggested that, in case of a future effusive eruption, the database of the pre-made simulations can be used to retrieve the simulations triggered at computational vents close to actual vent(s); these readily available simulations could serve as a proxy for the upcoming event. In the example shown by Crisci et al. (2010) the computational vents used as proxies are located at a distance up to ~0.5 km from the actual vent, and an analysis of the error introduced by this misplacement is desirable. In particular it could be interesting to explore how this kind of error varies throughout the varied morphology of the volcano.

To do this we use the simulation database of Favalli et al. (2009a) and quantify the maximum error obtained, locally, by considering a vent shift of a given distance from the correct position.

ACCEPTED MANUSCRIPT

This is done by quantifying how different are the simulations (re-loaded from the existing database) triggered at four computational vents constituting a square element with side σ (Figure 3), according to:

$$\delta = (s_1 \cap s_2 \cap s_3 \cap s_4)/(s_1 \cup s_2 \cup s_3 \cup s_4) \quad (7)$$

the δ value is attributed to the point n_i, which is the centroid a of a generic square element defined by the vents of simulations s_1, s_2, s_3, s_4 (Figure 3). δ varies between 0 and 1: it is 0 when the intersection is null and increases when the overlap of the four simulations increases (Figure 3). There are two parameters which need to be associated with a δ value: the side σ of the considered square element, and the lava flow length used to limit the extent of the DOWNFLOW simulation. The flow length must be substantially greater than σ, otherwise the value of δ will be affected. Provided this condition, δ can be calculated for increasing flow length, thus exploring how the behaviour evolves far from the vent. To simplify, here we have used a fixed maximum length of 4 km. In this case (shown in section 3.3) a complete notation for δ is $\delta_{(80m,\ 4km)}$. We call δ confluence/diffluence index. In fact, high values of δ mean that locally the lava flows have a very high tendency to converge and to flow along the same path. At the other end, a null value of δ means that at least one of the flows follows a path completely different from the others. The value δ given by equation (4) can thus be directly related to the expected error when a vent is misplaced by a length equal to the half diagonal of the square element considered.

We can obtain maps of the confluence/diffluence index by calculating the δ value over all the square elements of the mesh of the computational vents. In section 3.3 three confluence/diffluence maps are shown for increasing size of the side σ of the square elements considered.

3. Processing and results

ACCEPTED MANUSCRIPT

3.1. Reference hazard map

The reference map taken as test case is the one published by Favalli et al. (2009a) for Mount Etna. The basis for numerical simulations is a DEM of the volcano with a 10 m spatial resolution. For an area of 622 km^2 around the summit, the elevation data has been derived from an airborne LIDAR survey carried out in September 2005 (Figure 1). The average point density of the LIDAR return pulses was 0.41 points/m^2, with a nominal accuracy of ±0.4 m (vertical) and ±1.5 m (horizontal). The DEM outside the LIDAR survey has been derived from the digital regional cartography of the Sicily region at 1:10,000 scale (related survey dates back to 1998), and the relative root mean square error in elevation has been calculated in ~2 m (Neri et al., 2008; Tarquini et al., 2012). The mesh of computational vents is spaced 80 m and its coverage is shown in Figure 1. The reference spatial probability density function (PDF) of vent opening for future eruptions was assumed to be directly related to the position of past vents (Guest and Murray, 1979; Behncke et al., 2005). As also discussed in Favalli et al. (2009d), summit eruptions venting above ~3000 m asl are too short to pose a threat to inhabited areas, hence for hazard purposes the focus is mainly on flank eruptions. For this reason the considered vent opening PDF (white contours in Figure 1) does not really account for eruptions from the summit, but for the potentially dangerous future vent opening on the flanks of the volcano, and was obtained by applying a Gaussian smoothing kernel (bandwidth = 1 km) over a set of more than 400 points representing old vents (see Favalli et al., 2009d for details). The settings used for the DOWNFLOW code were the standards for Mount Etna, with Δh = 3 m and N = 10,000 (Tarquini and Favalli, 2011), while flow lengths were constrained according to the law shown in the lower inset of Figure 1.

3.2. Sensitivity to input settings

ACCEPTED MANUSCRIPT

The number of computational vents, and hence the spacing between them, is determined by the balance between computational requirements of the simulation code and the available computational resources: the higher the number of vents, the higher the number of simulations and the higher the computational resources required. A very low-demanding code such as DOWNFLOW allows setting-up of an array of more than 70,000 computational vents at Mount Etna (Favalli et al., 2009a), while more complex codes, so far, allowed the processing of much coarser layouts of computational vents (Table 1) even if dedicated facilities (e.g. Rongo et al., 2011) are used.

To explore the effect of variations in the computational vent spacing in the final hazard map, we sub-sampled the 80 m-spaced mesh of vents presented by Favalli et al. (2009a) obtaining hazard maps for computational vent meshes spaced 480, 960 and 1920 m (Figure 4).

In Figure 5 we apply three different PDF for future vent opening with respect to the one applied by Favalli et al. (2009a). The original PDF (white contours in Figure 1) was derived by applying a kernel smoothing technique to more than 400 points representing the vents of past flank eruptions (Favalli et al., 2009d). We obtain the three modified PDF by applying the same smoothing kernel over randomly-selected subsets of the original set of vents, containing only 80, 60 and 40 % of the original number (Figure 5).

In Figure 6 we examine the effects on hazard maps of three different functions for the expected length of the flows with respect to the one applied by Favalli et al. (2009a) and illustrated in the inset of Figure 1. In the original length distribution, flows starting at each vent elevation have a uniform probability distribution in length up to c_1, then the probability decreases linearly to 0 from c_1 to c_2. The three additional laws considered here are dependent upon vent elevation as follows: (i) flow lengths have a uniform probability distribution up to a maximum length c_1; (ii) flows lengths have uniform probability distribution up to a maximum length c_2; (iii) flows have the length probability distribution described in Favalli et al. (2009d), hence flows reach at least length 0.5 l_1 and then the probability decreases linearly to 0 at the length l_1, where the relation between the

ACCEPTED MANUSCRIPT

maximum length l_1 (m) and the elevation of the vent h_v (m) is $l_1 = -6.25h_v + 26{,}075$ (Favalli et al., 2009d).

The produced hazard maps are distributions of probability of the invasion by future lava flows. To quantify the deviations introduced by the variation in the input parameters we need a mean to evaluate the distance between two hazard maps. Considering these maps as functions of the plane ($h = h(x, y)$), distances commonly used are those derived from the L_1 norm and the L_2 norm. In our case, if Ω is the computational domain, the L_1 and L_2 norm of a function (a hazard map) $h(x,y)$ is defined by

$$N_{p,h} = \left(\int_{\Omega} |h(x,y)|^p \, dxdy \right)^{1/p} \tag{8}$$

in the case of p=1 and p=2 respectively. The corresponding L_1 and L_2 distance between 2 functions $h_a(x,y)$ and $h_b(x,y)$ is then defined by

$$D_{p,h_a,h_b} = \left(\int_{\Omega} |h_a(x,y) - h_b(x,y)|^p \, dxdy \right)^{1/p} \tag{9}$$

for p=1 and p=2 respectively. The region outside the computational domain contributes in a negligible way to the distance between the hazard maps.

In Table 2 the distances between the probability distribution of inundation derived here (Figures 4-6) and the reference one (Figure 1) are shown. The L_1 norm of an hazard map is expressed in m^2, and represent the expected area emplaced by the next lava flow

3.3. Confluence/diffluence maps for increasing vent spacing

We apply the algorithm described in section 2.5 to calculate confluence/diffluence maps for σ = 80, 240 and 480 m (Figure 7). The confluence/diffluence values δ (equation 7; Figure 3) quantify

ACCEPTED MANUSCRIPT

the worst fit expected (i.e. the highest error introduced) when the vent is misplaced within a given square element having side σ. The DOWNFLOW code is calibrated as usual for Mount Etna (e.g. Tarquini and Favalli, 2011), and the runout distance is fixed to 4 km, hence the diffluence maps of Figure 7 can be written as $\delta_{(80m,\ 4km)}$, $\delta_{(240m,\ 4km)}$ and $\delta_{(480m,\ 4km)}$. The pie diagrams at the bottom-left of each map summarize the coverage of different class of δ values in each diffluence map.

4. Discussion

4.1. Hazard maps settings

For each one of the considered input parameters we calculate different hazard maps obtained by varying input settings within ranges close to previously used values (row 1 in Figures 4, 5 and 6), then we calculate the difference with respect to the reference hazard map (row 2 in Figures 4, 5 and 6) and finally we calculate the same difference expressed in percent with respect to the value in the original map (row 3 in Figures 4, 5 and 6).

To better highlight the effect of changes in input settings, we use two masks to compute the differences between the maps only in selected portions of the whole computational domain. The first mask (mask1) allow the computation of the difference only where the probability in the hazard map of Figure 1 is > 1%. The second mask (mask2) allow computation of the difference only in pixels of the computational domain covered (partially or completely) by buildings. Both masks are shown in row 4 in Figures 4, 5 and 6 and are specifically considered in Table 2. In particular, the percentage errors introduced in the pixels occupied by buildings (mask 2) correspond to the percentage error on the risk maps if as value at risk we consider only the buildings.

4.1.1. Vent spacing

ACCEPTED MANUSCRIPT

The changes of the hazard map when the computational vent spacing increases from 80 m (Figure 1) to 480 m (panel 4a1) are locally significant at high to medium elevations (panel 4a2) but tend to decrease towards the more inhabited areas at lower elevations (panels 4a3, 4a4). At a vent spacing of 960 m (panel 4b1) the changes become more important, even if many regions at low elevations still show only moderate changes (panels 4b2, 4b3 and 4b4). At a vent spacing of 1920 m (panel 4c1) differences get greater and more widespread while lower elevations are still less affected by changes with respect to higher elevations (panels 4c2, 4c3 and 4c4). Table 2 further highlights this general trend. It is evident that for increasing computational vent spacing the overall L_1 percentage distance increases (as expected) while the L_1 percentage distance calculated in the regions where the inundation probabilities are >1% and covered by buildings (panels 4a4, 4b4 and 4c4) show substantially lower values compared to the overall L_1 percentage distance. It is evident in row 3 of Figure 4 that the relative change highlights the data removal at higher elevations which is the effect of a much sparser mesh of computational vents on a convex area such as the summit of the volcano. This results in the dominance of negative values. Nevertheless, this lack of information tends to be compensated downhill, where the increasing number of overlapping simulations partly rebalances the higher vent spacing and the overall lower number of simulations.

4.1.2. Input PDF

Row 2 of Figure 5 shows that by randomly reducing the information processed to derive the PDF for future vent opening, the resulting hazard maps (panels 5a1, 5b1 and 5c1) are affected by differences which are evenly distributed in negative and positive values. All the panels in rows 3 and 4 in Figure 5 further highlight that the same general pattern essentially holds even if relative differences (Figure 5, row 3) and partial domains (Figure 5, row 4) are considered. Values in Table 2 indicates the expected increase of the L_1 distance percent as the depletion of data considered in the input PDF increases, while for each PDF, L_1 distances percent tend to stay constant or slightly decrease when partial domains are considered. In Table 3 we compared the three modified PDF

ACCEPTED MANUSCRIPT

with the original one. It is noteworthy that the smoothing kernel applied tends to reduce the impact of the removing of considered features with the consequence that the L_1 distance percent values are always lower than the percent of removed input features (especially for higher features removals).

4.1.3. Flow length

A first glance at Figure 6 reveals that the flow length parameter seems more critical than the two previously considered parameters. As expected, all the difference maps (rows 2, 3 and 4 in Figure 6) show an essentially coherent sign: constantly lower probability of inundation for shorter flows (column a in Figure 6) and higher probability for longer flows (columns a and b in Figure 6). It is also evident that the differences are higher, on average, with respect to previous cases. A common, typical trend of all the difference maps in Figure 6 is that the difference regularly increases with the distance from the summit. This is an opposite pattern with respect to the one observed in Figure 4, where differences decrease at lower elevations (i.e. in densely inhabited areas). A very important consequence of this trend is that the L_1 distance percent increases substantially when the computational domain is restricted to buildings (Table 2).

Thus, the final length of the flows results to be a critical parameter because it introduces the highest changes in the hazard map. To check the consistency of the considered laws for the length of flows, we computed, for future flows over the whole volcano, the probability of reaching a runout length according to the 4 different laws considered, and we plot the result along with the runout probability calculated from a database of actual lava flows (Figure 8). The curve c_1 is in good agreement with the actual flows, while the law selected for the reference hazard map (curve c_1-c_2) results to be a conservative choice and overestimates by ~30% the overall hazard and by ~50% the hazard over buildings (Table 2); the law l_1, instead, introduces an even higher overestimation (see Table 2).

4.2. Impact quantification vs computational vent spacing

ACCEPTED MANUSCRIPT

Table 1 shows that the computational vent spacing is the main difference between the setup of the different cases considered. As mentioned in section 2.4, when approaching the evaluation of the expected impact upon given vent opening, the spacing between the computational vents defines the resolution of the obtained result. In Figure 9 we compare the expected impact on the village of Nicolosi presented by Crisci et al. (2010) with the one obtained by using the "reversed risk" concept introduced by Favalli et al. (2009a) and applied here on the same target (a polygon enclosing the village). The two setups yield a substantially different information in terms of resolution.

When the simulations processed to derive the hazard maps are used as proxies for possible future eruptions, the confluence/diffluence index introduced in section 2.5 is a mean to fruitfully approach the involved uncertainty. In Figure 10 we consider the hypothetical future eruption from an extensive system of fissures on the East-Nordest flank of the volcano presented by Crisci et al. (2010) where the fissures have been approximated by the 16 nearest computational vents in the database (Figure 10a). By overlaying this scenario onto the maps of the confluence/diffluence index of Figure 7 it is possible to assess at each point along the eruptive fissures the error introduced by misplacing the vent by a distance σ (Figure 10b-d). It is noteworthy that when the grid of computational vent is spaced 80 m (σ = 80 m, Figure 10b) the maximum error introduce by approximating the actual vents with the nodes of the grid is mostly between 30 and 50%; in contrast, when the grid of computational vent is spaced 480 m (σ = 480 m, Figure 10d) the maximum error introduce by approximating the actual vents with the nodes of the grid is mostly between 80 and 100%,

5. Conclusions

ACCEPTED MANUSCRIPT

By using the DOWNFLOW code (Favalli et al., 2005), we explored how different settings of three input parameters are reflected in a hazard map of lava flows for Mount Etna. The cell size of the mesh of computational vents (hence the number of computational vents) do not affect substantially the obtained probability of inundation, provided that it does not exceed ~0.5 km. In particular it is noteworthy that the effect of an increase in vent spacing tends to be compensated in the lower flanks of the volcano, which are also the more densely populated areas. The effect of changes in the PDF for future vent opening is significant but it does not introduce abrupt changes since the random removal of 20%, 40% and 60% of the information used to create the input PDF results, respectively, in changes of ~10%, ~12.5% and ~17% (on average) in the final hazard map. In contrast, the length of future lava flows results to be a critical parameter: the difference between the reference hazard map (Favalli et al. 2009a) and the l_1 law hazard map (Favalli et al. 2009d) is ~65% over the whole computational domain, and ~95% if the difference is computed only over the areas covered by buildings.

We showed that while for the making of a global hazard map for lava flows a mesh of computational vent spaced 240 m provides a precise probability of being struck by a future flow, when the target is to forecast specific, local scenarios a small error in vent position can produce a biased result. This effect is quantified at each point of the volcano by the presented maps of confluence/diffluence index.

Although the obtained results have been obtained by using only the DOWNFLOW code (Favalli et al., 2005), we showed that the procedure followed for the derivation of a lava flow hazard map by using different lava flow simulation codes, i.e. SCIARA (Rongo et al., 2011) and MAGFLOW (Cappello et al., 2011a), are substantially equivalent. Accordingly, results can constitute a reference to set up similar maps using different simulation codes at Mount Etna and elsewhere.

Acknowledgments

ACCEPTED MANUSCRIPT

The authors wish to thank two anonymous reviewer which improved the quality of the manuscript. This study was partially supported by the Italian Dipartimento della Protezione Civile (DPC) in the framework of a 2007-2009 agreement with the Istituto Nazionale di Geofisica e Vulcanologia (INGV). Scientific papers supported by the DPC do not represent its official opinion and policies.

References

Barberi, F., Carapezza, M.L., Valenza, M., and Villari, L., 1993, The control of lava flow during the 1991–1992 eruption of Mt. Etna: Journal of Volcanology and Geothermal Research, v. 56, p. 1–34, doi: 10.1016/0377-0273(93)90048-V.

Barca, D., Crisci, G. M., Rongo, R., Di Gregorio, S., Spataro, W., 2004. Application of the Cellular Automata Model SCIARA to the 2001 Mount Etna Crisis, in Mount Etna: Volcano Laboratory, Geophys. Monogr. Ser., vol. 143, edited by A. Bonaccorso et al., pp. 343–356 AGU, Washington, D. C.

Behncke, B., M. Neri, and A. Nagay (2005), Lava flow hazard at Mount Etna (Italy): New data from a GIS-based study, in Kinematics and dynamics of lava flows. Geological Society of America Special Paper, 396, edited by M. Manga, and G. Ventura, 189–208.

Bilotta, G., Rustico, E., Hérault, A., Vicari, A., Russo, G., Del Negro, C., Gallo, G., 2011. Porting and optimizing MAGFLOW on CUDA. Annals of Geophysics 54, 580–591, http://dx.doi.org/10.4401/ag-5341.

Cappello, A., Vicari, A., Del Negro, C., 2011a. Retrospective validation of a lava-flow hazard map for Mount Etna volcano. Annals of Geophysics 54, 634–640, http://dx.doi.org/10.4401/ag-5345.

Cappello, A., Vicari, A., Del Negro, C., 2011b. Assessment and modeling of lava flow hazard on Mt. Etna volcano. Bollettino di Geofisica Teorica ed Applicata 52, http://dx.doi.org/10.4430/bgta0003.

Chirico, G.D., Favalli, M., Papale, P., Boschi, E., Pareschi, M.T., Mamou-Mani, A., 2009. Lava flow hazard at Nyiragongo volcano, D.R.C. 2. Hazard reduction in urban areas. Bull. Volcanol. 71, 375-387, doi:10.1007/s00445-008-0232-z.

Calvari, S., Behncke, B., 2006. Etna: lava flows from multiple vents during 22 September to 4 November. Bull. Glob. Volcanism Netw. 31 (10), 2–3.

Costa, A., Macedonio, G., 2005a, Computational modeling of lava fl ows: A review, in Manga, M., and Ventura, G., eds., Kinematics and dynamics of lava flows: Geological Society of America Special Paper 396, p. 209–218. doi: 10.1130/2005.2396(14).

Costa, A., Macedonio, G., 2005b. Numerical simulation of lava flows based on depth-averaged equations. Geophys. Res. Lett. 32, L05304, doi:10.1029/2004GL021817.

Crisci G.M., Di Gregorio, S., Rongo, R., Scarpelli, M., Spataro, W., Calvari, S., 2003. Revisiting the 1669 Etnean eruptive crisis using a cellular automata model and implications for volcanic hazard in the Catania area. Journal of Volcanology and Geothermal Research 123, 211-230.

Crisci, G.M., Rongo, R., Di Gregorio, S., Spataro,W., 2004. The simulationmodel SCIARA: the 1991 and 2001 lava flows at Mount Etna. J. Volcanol. Geotherm. Res. 132, 253–267.

Crisci, G.M., Iovine, G., Di Gregorio, S., Lupiano, V., 2008. Lava flow hazard on the SE flank of Mt. Etna (Southern Italy). J. Volcanol. Geotherm. Res. 177, 778–796.

Crisci, G. M., Avolio, M. V., Behncke, B., D'Ambrosio, D., Di Gregorio, S., Lupiano, V., Neri, M., Rongo, R., Spataro, W., 2010. Predicting the impact of lava flows at Mount Etna, Italy, J. Geophys. Res., 115, B04203, doi:10.1029/2009JB006431.

ACCEPTED MANUSCRIPT

Del Negro, C., Fortuna, L., Vicari, A., 2005. Modelling lava flows by Cellular Nonlinear Networks (CNN): preliminary results. Nonlinear Process. Geophys. 12, 505–513.

Favalli, M., Pareschi, M.T., Neri, A., Isola, I., 2005. Forecasting lava flow paths by a stochastic approach. Geophys. Res. Lett. 32, L03305, doi:10.1029/2004GL021718.

Favalli, M., Chirico, G.D., Papale, P., Pareschi, M.T., Coltelli, M., Lucana, N., Boschi, E., 2006. Computer simulations of lava flow paths in the town of Goma, Nyiragongo volcano, Democratic Republic of Congo. J. Geophys. Res. 111. doi: 10.1029/2004JB003527.

Favalli, M., Tarquini, S., Fornaciai, A., Boschi, E., 2009a. A new approach to risk assessment of lava flow at Mount Etna. Geology 37, 1111–1114.

Favalli, M., Fornaciai, A., Pareschi, M.T., 2009b. LIDAR strip adjustment: Application to volcanic areas. Geomorphology 111, 123–135, doi:10.1016/j.geomorph.2009.04.010.

Favalli, M., Chirico, G.D., Papale, P., Pareschi, M.T., Boschi, E., 2009c. Lava flow hazard at Nyiragongo volcano, D.R.C. 1. Model calibration and hazard mapping. Bull. Volcanol. 71, 363–374. doi:10.1007/s00445-008-0233-y.

Favalli, M., Mazzarini, F., Pareschi, M.T., Boschi, E., 2009d. Topographic control on lava flow paths at Mt. Etna (Italy): implications for hazard assessment. J. Geophys. Res. 114 F01019. doi:10.1029/2007JF000918.

Favalli, M., Tarquini, S., Fornaciai, A., 2011. DOWNFLOW code and Lidar technology for lava flow analysis and hazard assessment at Mount Etna. Annals of Geophysics 54, 552–566, http://dx.doi.org/10.4401/ag-5339.

Favalli, M., Tarquini, S., Papale, P., Fornaciai, A., Boschi, E., 2012. Lava flow hazard andrisk maps at Mount Cameroon volcano. Bulletin of Volcanology 74, 423–439. doi:10.1007/s00445-011-0540-6.

Felpeto, A., Arana, V., Ortiz, R., Astiz, M., Garcia, A., 2001. Assessment and modelling of lava flow hazard on Lanzarote (Canary Islands), Natural Hazards, 23, 247–257.

Guest, J.E., Murray, J.B., 1979. An analysis of hazard from Mount Etna volcano. Journal of the Geological Society of London 136, 347-354.

Guest, J.E., 1982. Styles of eruption and flow morphology on Mount Etna. Mem. Soc. Geol. Ital., 23, 49–73.

Herault, A., Bilotta, G., Vicari, A., Rustico, E., Del Negro, C., 2011. Numerical simulation of lava flow using a GPU SPH model. Annals of Geophysics 54, 600–620. http://dx.doi.org/10.4401/ag-5343.

Hidaka, M., Goto, A., Umino, S., Fujita, E., 2005. VTFS project: Development of the lava flow simulation code LavaSIM with a model for three-dimensional convection, spreading, and solidification. Geochem. Geophys. Geosyst., 6, Q07008, doi:10.1029/2004GC000869.

Kauahikaua, J., Margriter, S., Lockwood, J., Trusdell, F., 1995. Applications of GIS to the estimation of lava flow hazard on Mauna Loa Volcano, Hawaii, in Rhodes, J.M., and Lockwood, J.P., eds., Mauna Loa revealed: Structure, composition, history, and hazards: American Geophysical Union Geophysical Monograph 92, p. 315–325.

Kelman, I., Mather, T.A., 2008. Living with volcanoes: The sustainable livelihoods approach for volcano-related opportunities. Journal of Volcanology and Geothermal Research 172, 189-198. doi:10.1016/j.jvolgeores.2007.12.007.

Macedonio, G., Pareschi, M.T., Santacroce, R., 1990. A simple model for lava hazard assessment: Mount Etna, paper presented at International Volcanological Congress, Int. Assoc. of Volcanol. and Chem. of the Earth's Inter., Mainz, Germany, Sept.

Miyamoto, H., Sasaki, S., 1997. Simulating lava flows by an improved cellular automata method. Comput. Geosci. 23 (3), 283–292.

ACCEPTED MANUSCRIPT

Neri, M., Mazzarini, F., Tarquini, S., Bisson, M., Isola, I., Behncke, B., Pareschi, M.T., 2008. The changing face of Mount Etna's summit area documented with Lidar technology. Geophys. Res. Lett. 35, L09305, doi:10.1029/2008GL033740.

Proietti, C., Coltelli, M., Marsella, M., Fujita, E., 2009. A quantitative approach for evaluating lava flow simulation reliability: LavaSIM code applied to the 2001 Etna eruption. Geochem. Geophys. Geosyst., 10 Q09003, doi:10.1029/2009GC002426.

Pyle, D.M., 1995. Volcanoes – Reduction of urban hazards. Nature 378, 134-135. doi:10.1038/378134a0.

Renshler, C.S., 2005. Scales and uncertainties in using models and GIS for volcano hazard prediction. J. Volcanol. Geotherm. Res. 139, 73–87. doi:10.1016/j.jvolgeores.2004.06.016.

Rongo, R., Avolio, M.V., Behncke, B., D'Ambrosio, D., Di Gregorio, S., Lupiano, V., Neri, M., Spataro, W., Crisci, G.M., 2011. Defining high-detail hazard maps by a cellular automata approach: application to Mount Etna (Italy). Annals of Geophysics 54, 568–578, http://dx.doi.org/10.4401/ag-5340.

Salvi, F., Scandone R., Palma, C., 2006. Statistical analysis of the historical activity of Mount Etna, aimed at the evaluation of volcanic hazard. J. Volcanol. Geoth. Res. 154, 159-168.

Simkin, T., Siebert, L., Blong, R., 2001. Policy forum: Disasters - Volcano fatalities - Lessons from the historical record Source: Science 291, 255-255. doi:10.1126/science.291.5502.255.

Smethurst L., James, M.R., Pinkerton, H., Tawn, J.A., 2009. A statistical analysis of eruptive activity on Mount Etna, Sicily. Geophys. J. Int., 179, 655-666.

Tarquini, S., Isola, I., Favalli, M., Mazzarini, F., Bisson, M., Pareschi, M.T., Boschi, E., 2007. TINITALY/01: A new Triangular Irregular Network of Italy. Ann. Geophys. 50, 407–425.

Tarquini, S., Favalli, M., 2010. Changes of the susceptibility to lava flow invasion induced by morphological modifications of an active volcano: the case of Mount Etna, Italy. Natural Hazards 54, 537–546, doi:10.1007/s11069-009-9484-y.

Tarquini, S., Favalli, M., 2011. Mapping and DOWNFLOW simulation of recent lava flow fields at Mount Etna. Journal of Volcanology and Geothermal Research 204, 27–39, http://dx.doi.org/10.1016/j.jvolgeores.2011.05.001.

Tarquini, S., Vinci, S., Favalli, M., Doumaz, F., Fornaciai, A., Nannipieri, L., 2012. Release of a 10-m-resolution DEM for the Italian territory: comparison with globalcoverage DEMs and anaglyph-mode exploration via the web. Computers & Geosciences 38, 168–170, http://dx.doi.org/10.1016/j.cageo.2011.04.018.

Vicari, A., Ganci, G., Behncke, B., Cappello, A., Neri, M., Del Negro, C., 2011a. Near-real-time forecasting of lava flow hazards during the 12–13 January 2011 Etna eruption. Geophys. Res. Lett., 38, L13317. doi:10.1029/2011GL047545.

Vicari, A., Bilotta, G., Bonfiglio, S., Cappello, A., Ganci, G., Hérault, A., Rustico, E., Gallo, G., Del Negro, C., 2011b LAV@HAZARD: a web-GIS interface for volcanic hazard assessment. Annals of Geophysics 54, 662–670. http://dx.doi.org/10.4401/ag-5347.

Wadge, G., Young, P.A.V., McKendrick, I.J., 1994. Mapping lava flow hazards using computer simulation, J. Geophys. Res., 99, 489– 504.

ACCEPTED MANUSCRIPT

Figure Captions

Figure 1. Map of the probability of lava flow inundation by flank eruptions at Mount Etna (after Favalli et al., 2009a). White contour lines show the probability distribution of future vent opening (%/km^2). The area covered by the grid of computational vents is enclosed by the dotted blue line. The topography is represented by a merge of the TINITALY DEM (Tarquini et al., 2007; 2012) and the 2005 LIDAR-derived DEM (inside the dashed white line, Favalli et al., 2009b). The bottom right inset is the plot of lava flow length vs. vent elevations. Red dots show the distribution of past lava flows. Curves c_1 and c_2 (black dashed lines) are used for computation of expected lava flow lengths: for any given vent elevation, we assume that the lava flow has a uniform probability of attaining any length up to curve c_1, then this probability decreases linearly to zero from c_1 to c_2. For interpretation of the references to colour in this figure legend, the reader is referred to the web version of this article.

Figure 2. Output of a DOWNFLOW simulation. a) Simulation of the lava flow emplaced from a vent opened at SW from the South East Crater on 26 October 2006 at an elevation ~3050 m. The position of the vent (labeled v) has been set according to Calvari and Behncke (2006). Color table highlights different number *n* of paths per pixels (increasing from dark red to yellow). b) The same simulation of a) with a color table showing downflow distance from the vent; each downflow distance is attributed with a probability of inundation according to Favalli et al. (2009a; see Figure 1). White contours show the actual flow field; SEC = South East Crater. c) Expected lava flow length and probability of inundation for a vent at an elevation of 3050 m. In black, length probability distribution for a lava flow venting at such an elevation (from Favalli et al., 2009a) and, in red, the corresponding probability of inundation as a function of the downflow distance L from the vent. Blue line shows the average expected length. Vertical dotted lines mark lengths c_1 and c_2 (see Figure 1). For interpretation of the references to colour in this figure legend, the reader is referred to the web version of this article.

Figure 3. Conceptual scheme for the computation of the confluence/diffluence index. Starting from the mesh of computational vents (black circles), a square element having side σ is identified by the vents of four simulations s_1, s_2, s_3, s_4 **(**vents are represented by yellow, blue, green and red colored circles; simulations by the related colored polygons which are the subject of intersections and unions in equation 7). The δ value is calculated using equation (7) and attributed to the centroid of the square element. For the centroid n_i, the δ value will be high (close to unity) since the flows converge almost perfectly (confluence), while for n_j the δ value will be 0 since the flows are divergent (diffluence). Calculating the values of δ for all the square elements with side σ of the computational vent mesh we obtain a map of the confluence/diffluence index (with nodes represented by the orange circles). For interpretation of the references to colour in this figure legend, the reader is referred to the web version of this article.

Figure 4. Effects of variations in vent spacing on lava flow hazard maps at Mount Etna. Panels are organized in four rows (numbers 1 to 4) and three columns (letters a to c). The three columns refer to different input values of the computational vents spacing: 480, 960 and 1920 m for column a, b and c respectively. Row 1 shows the hazard maps, labeled H480, H960 and H1920 after the corresponding input vent spacing. Row 2 shows the difference between the hazard map with modified vent spacing and the reference map (H80, with a vent spacing of 80 m). Row 3 shows the relative difference (in percent) with respect to the reference map. In row 4 the relative difference (as in row 3, in percent) is shown only for the areas with a probability of inundation > 1% in the reference hazard map; green areas indicates buildings. For interpretation of the references to colour in this figure legend, the reader is referred to the web version of this article.

ACCEPTED MANUSCRIPT

Figure 5. Effects of variations in the PDF for future vent opening on lava flow hazard maps at Mount Etna. Panels are organized in four rows (numbers 1 to 4) and three columns (letters a to c). The three columns refer to different input distributions for future vent opening, calculated by considering only 80%, 60% and 40% of the original input features (column a, b and c respectively). Row 1 shows the hazard maps, labeled H_{PDF80}, H_{PDF60} and H_{PDF40}. Row 2 shows the difference between the hazard map of row 1 and the reference map H80. Row 3 shows the relative difference (in percent) of the maps in row 1 with respect to the reference map. In row 4 the relative difference (as in row 3, in percent) is shown only for the areas with a probability of inundation > 1% in the reference hazard map; green areas indicates buildings. For interpretation of the references to colour in this figure legend, the reader is referred to the web version of this article.

Figure 6. Effects of variations in the expected flow length distribution on lava flow hazard maps at Mount Etna. Panels are organized in four rows (numbers 1 to 4) and three columns (letters a to c). The three columns refer to the different expected flow length distribution used as input, labeled with the subscripts *c1*, *c2* and *l1* (column a, b and c respectively; see main text for explanation). Row 1 shows the hazard maps Hc_1, Hc_2 and Hl_1. Row 2 shows the difference between the hazard map of row 1 and the reference map H80. Row 3 shows the relative difference (in percent) of the maps in row 1 with respect to the reference map. In row 4 the relative difference (as in row 3, in percent) is shown only for the areas with a probability of inundation > 1% in the reference hazard map; green areas indicates buildings. For interpretation of the references to colour in this figure legend, the reader is referred to the web version of this article.

Figure 7. Maps of the confluence/diffluence index $\delta_{(80m,\ 4km)}$, $\delta_{(240m,\ 4km)}$ and $\delta_{(480m,\ 4km)}$ for Mount Etna calculated by elaborating the database of simulations of Favalli et al. (2009a) as explained in the main text. The black dotted contour encloses the area covered by the 80 m-spaced mesh of computational vents. Pie diagrams show the areal percentage distribution of the confluence/diffluence classes shown in the maps. For interpretation of the references to colour in this figure legend, the reader is referred to the web version of this article.

Figure 8. Plot of the probability of inundation as a function of the runout distance from the vent. Data have been computed for the whole volcano on the basis of the 4 different laws for expected flow lengths considered, and the plot for the length of real flows has been computed from the database of runouts shown in the bottom right inset of Figure 1.

Figure 9. Expected impact on the town of Nicolosi as a function of vent position. Loosely-spaced, white points with black contour (34 in total) are the computational vents, belonging to the simulation mesh of Crisci et al. (2010), which can affect the urban area of Nicolosi (red contour). The dense mesh of small, colored points (5586 in total) are the subset of the mesh of computational vents used by Favalli et al. (2009a) which can affect the same urban area. Beyond the simple Boolean information "is there an impact: Yes/No", the different colors used by Favalli et al. (2009a) quantify the expected impact in terms of squared meters of urban surface inundated. Buildings are in black; elevation contours in white; SEC = South East Crater. For interpretation of the references to colour in this figure legend, the reader is referred to the web version of this article.

Figure 10. The opening of a fissure system on the N-NE flank of the Volcano hypothesized by Crisci et al. (2010). a) scenario obtained by selecting the nearest computational vents from the grid of computational vents (modified after Crisci et al., 2010); the dotted frame *r* encloses the area shown in a), b) and c). Panels b-c-d: the fissure system and the computational vents overlain to the three confluence/diffluence maps shown in Figure 7. The length of σ is shown in each case, and allows a straightforward evaluation of the uncertainties introduced when the fissure system is

ACCEPTED MANUSCRIPT

approximated by the computational vents. For interpretation of the references to colour in this figure legend, the reader is referred to the web version of this article.

ACCEPTED MANUSCRIPT

ACCEPTED MANUSCRIPT

Table 1. Input settings for recent lava flow hazard maps for Mount Etna

Reference	Simulation code	Vent spacing (m)[a]	Number of vents	Simulations per vent	Cumulative number of simulations	Area of possible venting (km^2)
Crisci et al., 2008	SCIARA	1000	88	12	1056	~80
Favalli et al., 2009d	DOWNFLOW	80	~50,000	1*	~50,000	320
Favalli et al., 2009a	DOWNFLOW	80	~70,000	1*	~70,000	450
Crisci et al., 2010	SCIARA	707	393	100	39,300	~160
Tarquini and Favalli 2010	DOWNFLOW	80	~32,000	1*	~32,000	~200
Cappello et al., 2011a	MAGFLOW	500	4290	6	25,740	1100
Cappello et al., 2011b	MAGFLOW	1000	>900	6	>5400	[b]
Favalli et al., 2011	DOWNFLOW	500	4290	1*	4290	1100
Rongo et al., 2011	SCIARA	500	4290	6	25,740	1100

[a] Vents are always arranged in regular, square grids. All the grids are arranged in S-N trending columns and E-O trending rows with the exception of Crisci et al. (2010), where columns are trending SW-NE and rows SE-NW.

[b] Not specified.

* When a "single simulation" obtained with DOWNFLOW is used to derive a hazard map, different runout distances are weighted by assigning a probability function for the expected flow length. Hence a single output does not represent only a "single" event, but it accounts for a spectrum of possible events.

ACCEPTED MANUSCRIPT

ACCEPTED MANUSCRIPT

Table 2. Differences between probability distributions derived here and the reference ones.

	Inundation probability distribution	Considered domain	L_1 norm (m^2)	L_1 distance (m^2)	L_1 distance %	L_2 distance %
Vent spacing	H240	all	7,365,700	257,487	3.5	0.12
		>1%	5,506,026	124,315	2.3	0.08
		buildings	590,549	15,560	2.6	0.07
	H480	all	7,400,564	608,822	8.3	0.68
		>1%	5,527,790	308,446	5.6	0.49
		buildings	601,273	33,964	5.7	0.32
	H960	all	7,451,523	1,507,985	20.4	4.33
		>1%	5,597,061	818,763	14.8	3.27
		buildings	620,584	77,541	13.0	1.82
	H1920	all	7,416,930	3,623,359	49.1	31.3
		>1%	5,479,519	2,075,945	37.6	23.1
		buildings	622,186	186,023	31.3	11.0
Probability density function	H_{PDF80}	all	7,302,735	732,000	9.9	1.17
		>1%	5,517,480	509,818	9.2	1.11
		buildings	606,631	60895	10.2	1.15
	H_{PDF60}	all	7,428,084	999,117	13.5	2.27
		>1%	5,638,448	679,106	12.3	2.16
		buildings	564,849	63,143	10.6	1.72
	H_{PDF40}	all	7,360,663	1,366,864	18.5	3.79
		>1%	5,557,476	897,817	16.3	3.43
		buildings	556,666	93,162	15.7	2.75
Flow length law	Hc_1	all	4,972,966	2,406,002	32.6	12.6
		>1%	3,796,471	1,726,434	31.3	11.9
		buildings	304,758	289,958	48.8	21.8
	Hc_2	all	8,931,825	1,552,857	21.0	5.17
		>1%	6,637,562	1,114,657	20.2	4.86
		buildings	776,946	182,230	30.6	8.54
	Hl_1	all	12,214,603	4,838,310	65.6	51.1
		>1%	9,230,912	3,708,007	67.1	50.6
		buildings	1,155,401	560,874	94.3	85.7

ACCEPTED MANUSCRIPT

Table 3. Differences between the PDFs for future vent openings with respect to the reference one.

Input vent opening PDF	**Considered domain**	**removed vents (%)**	**L_1 distance**	**L_1 distance %**	**L_2 distance %**
PDF_{80}	all	20	0.20	19.6	10.4
PDF_{60}	all	40	0.27	27.4	14.8
PDF_{40}	all	60	0.39	39.3	23.8

ACCEPTED MANUSCRIPT

ACCEPTED MANUSCRIPT

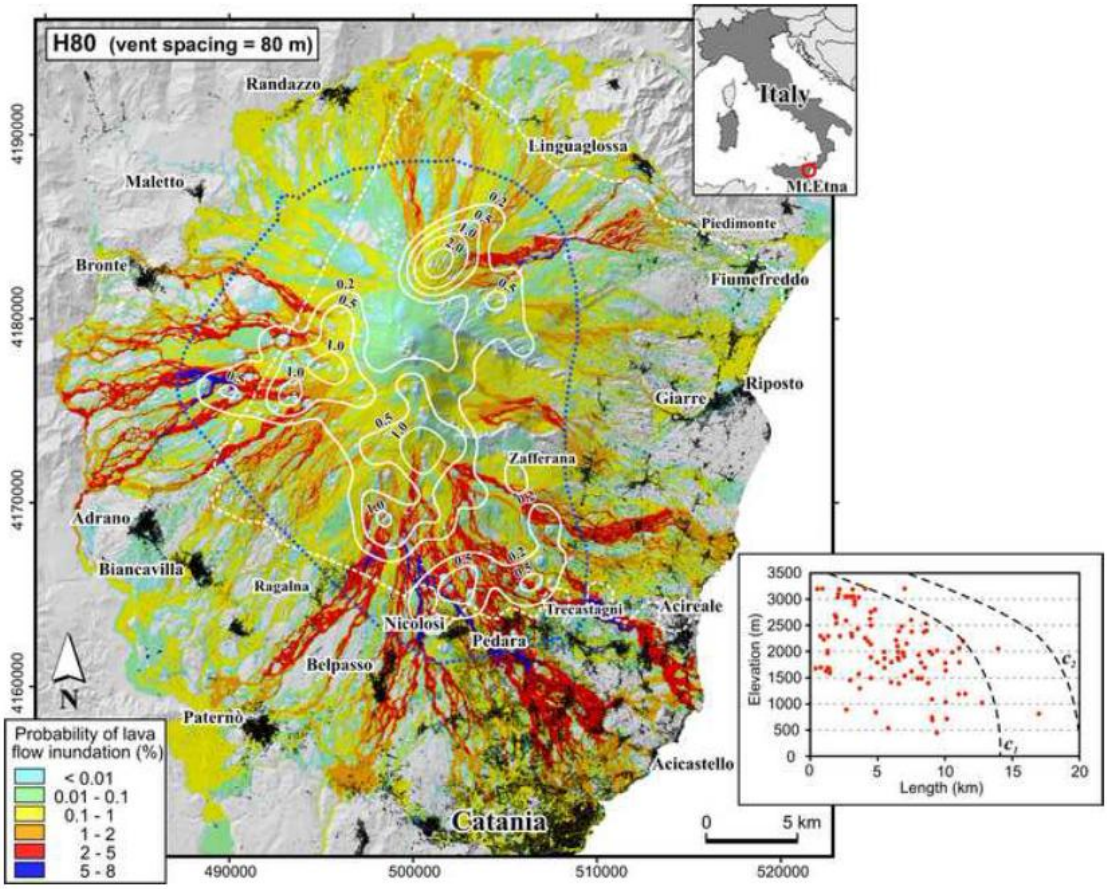

Figure 1

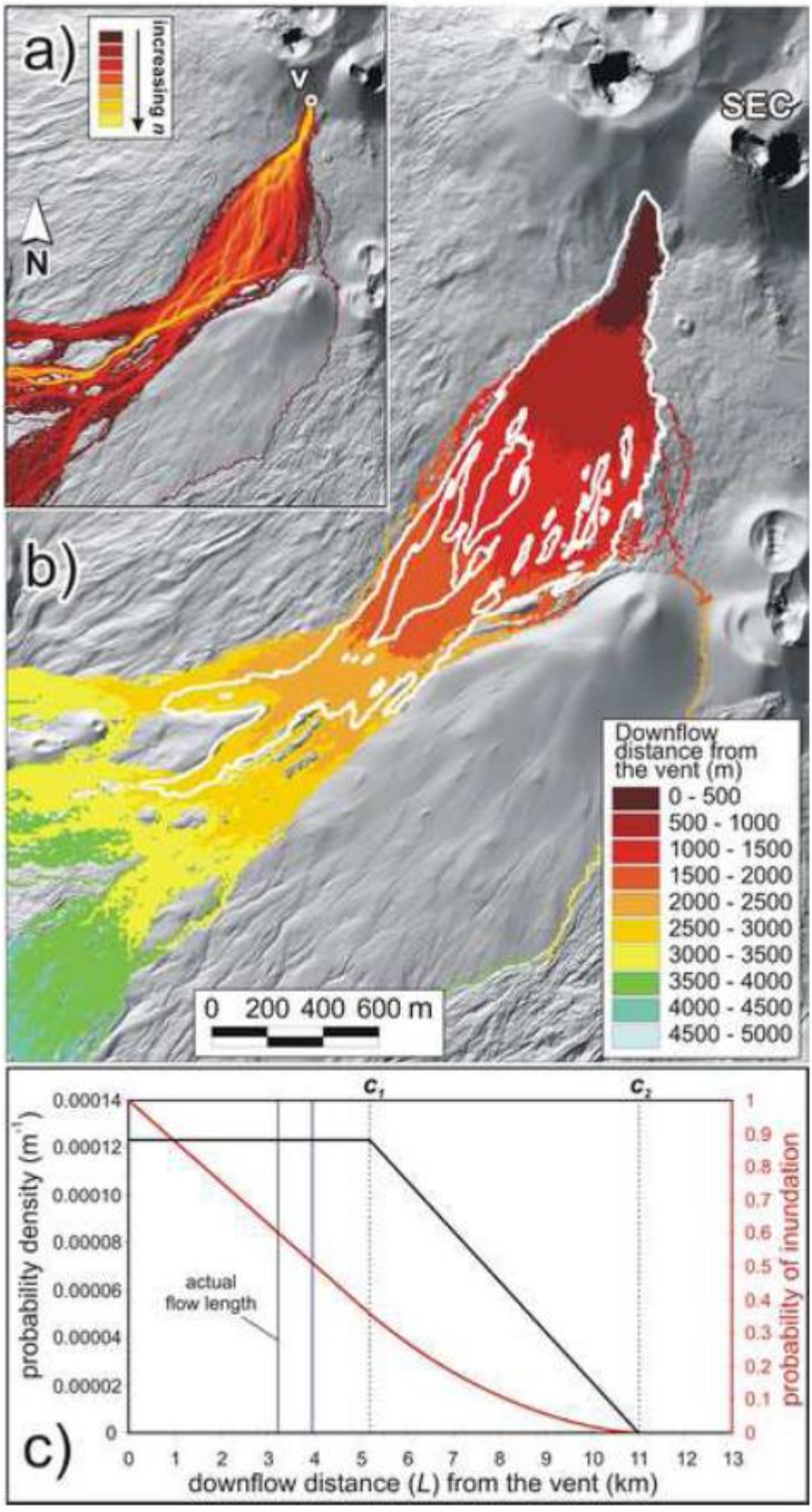
a)
increasing n
V
N
SEC
b)
Downflow distance from the vent (m)
0 - 500
500 - 1000
1000 - 1500
1500 - 2000
2000 - 2500
2500 - 3000
3000 - 3500
3500 - 4000
4000 - 4500
4500 - 5000
0 200 400 600 m
c)
c1
c2
probability density (m-1)
probability of inundation
actual flow length
downflow distance (L) from the vent (km)

Figure 2

ACCEPTED MANUSCRIPT

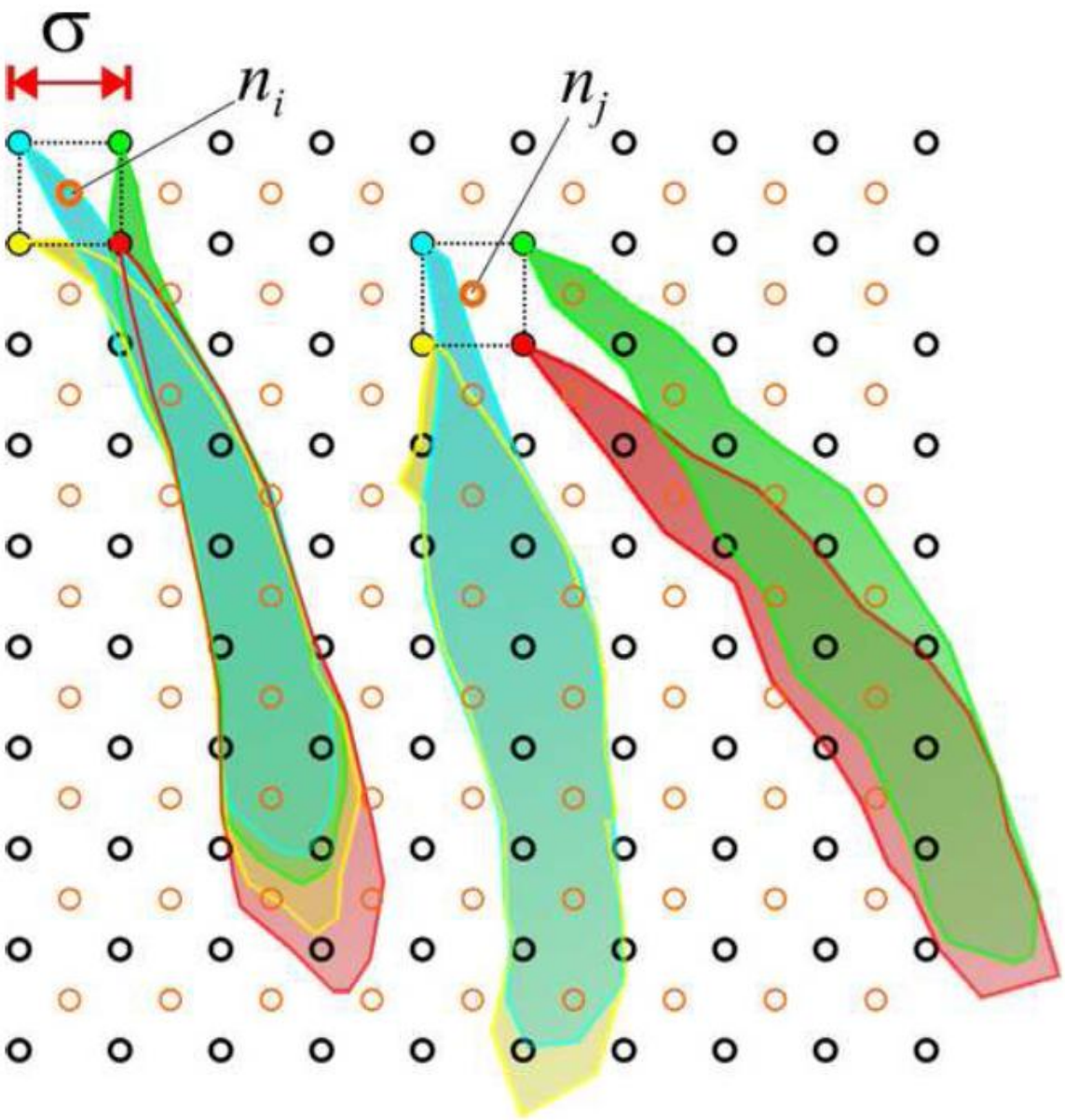

Figure 3

ACCEPTED MANUSCRIPT

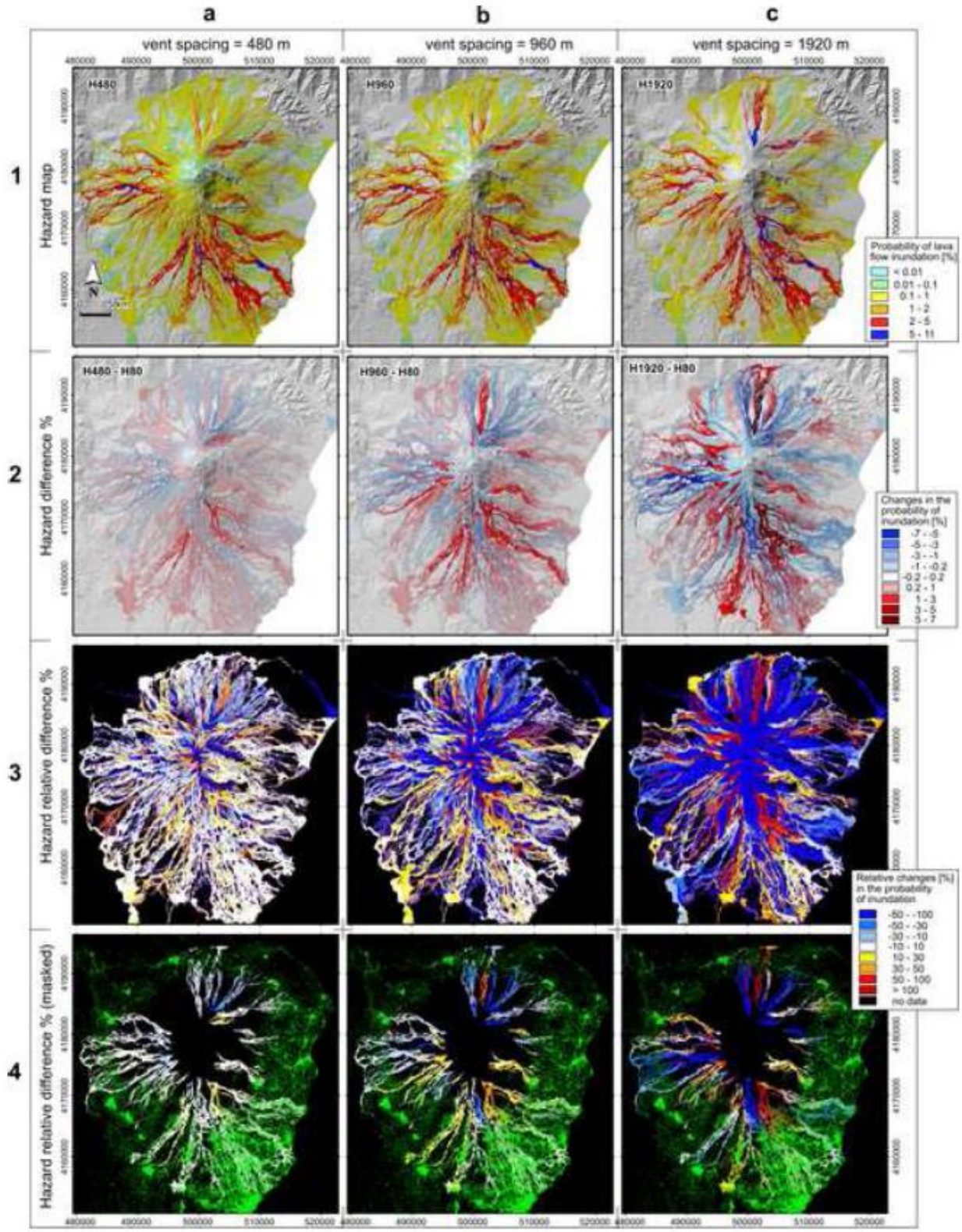

Figure 4

ACCEPTED MANUSCRIPT

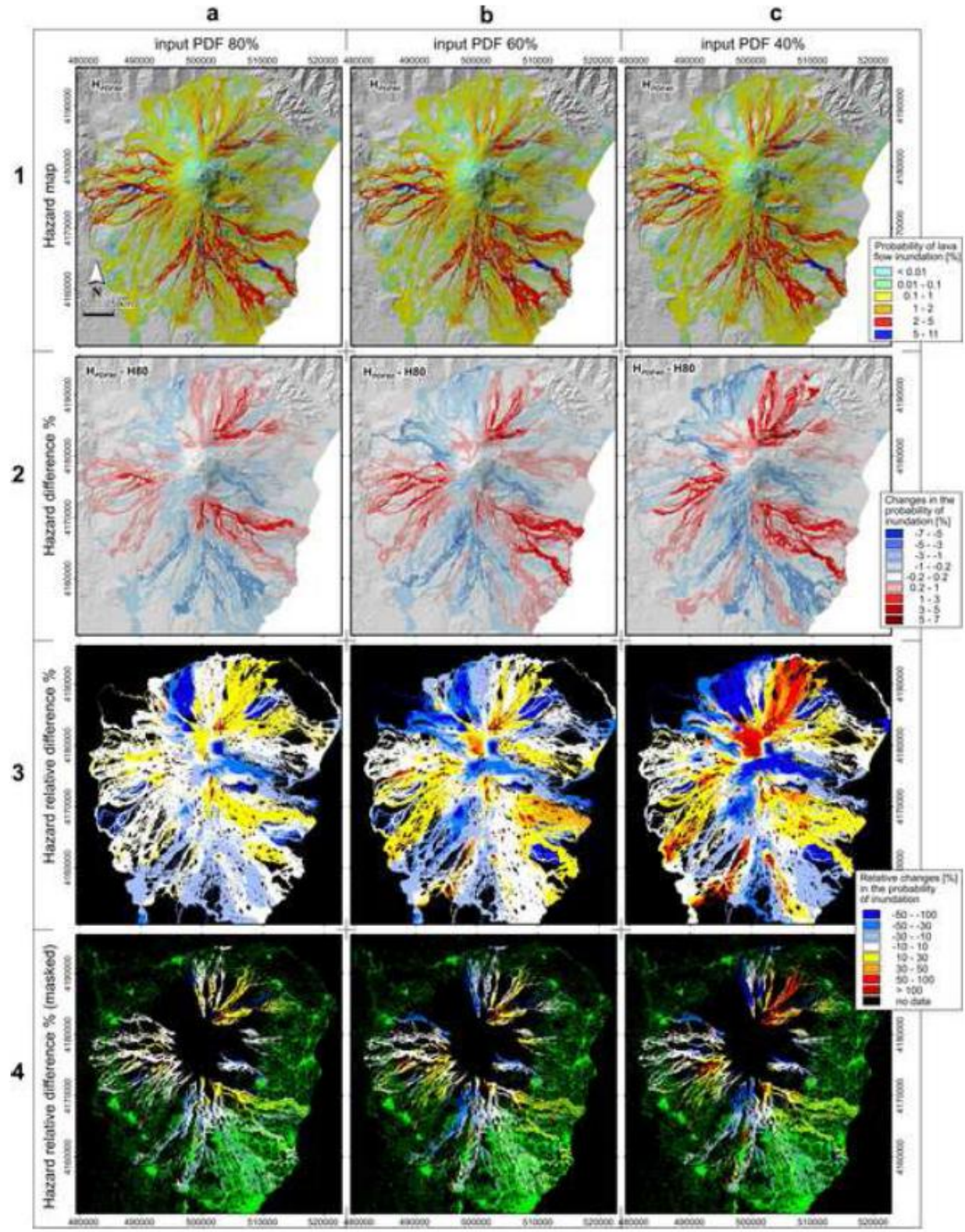

Figure 5

ACCEPTED MANUSCRIPT

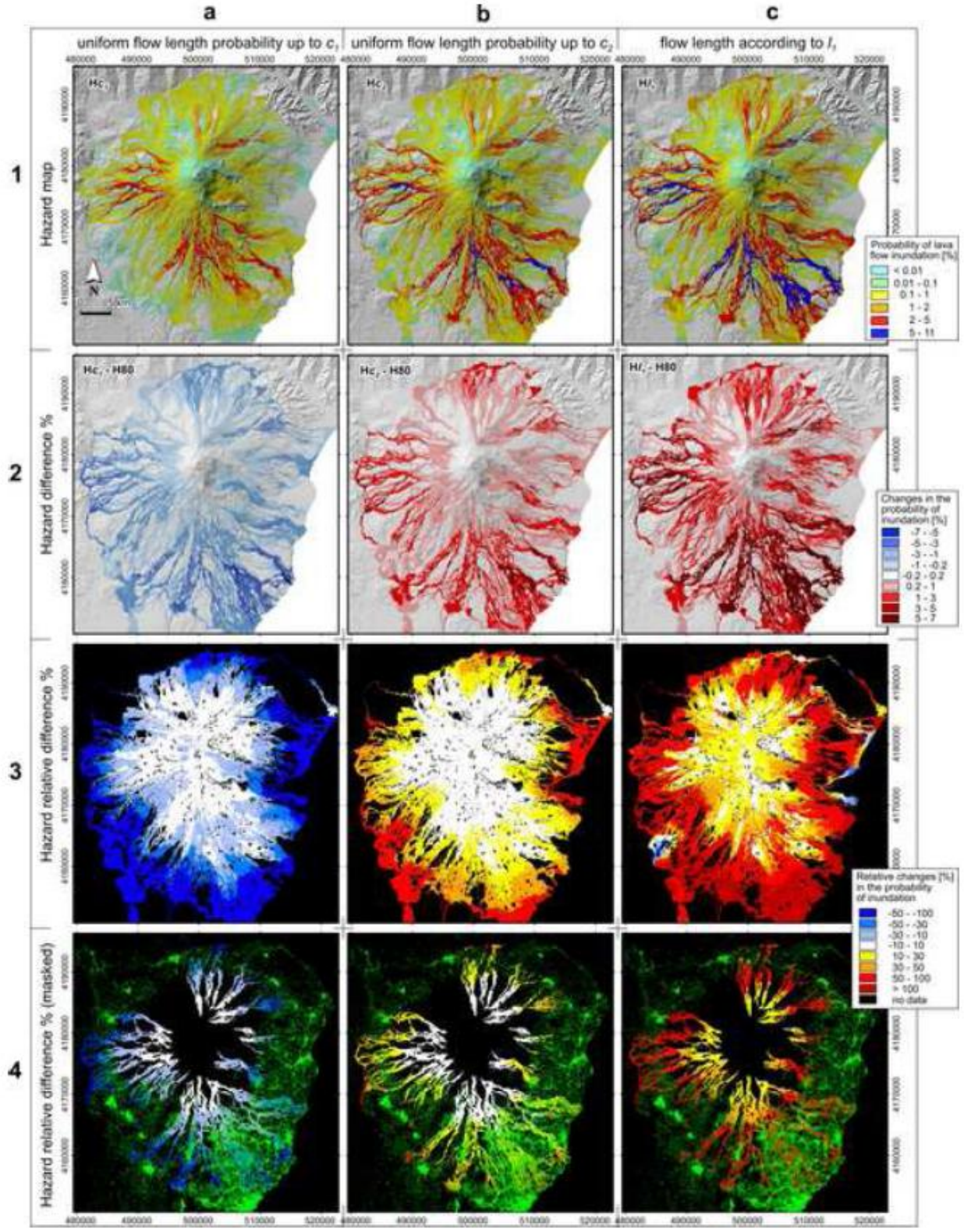

Figure 6

ACCEPTED MANUSCRIPT

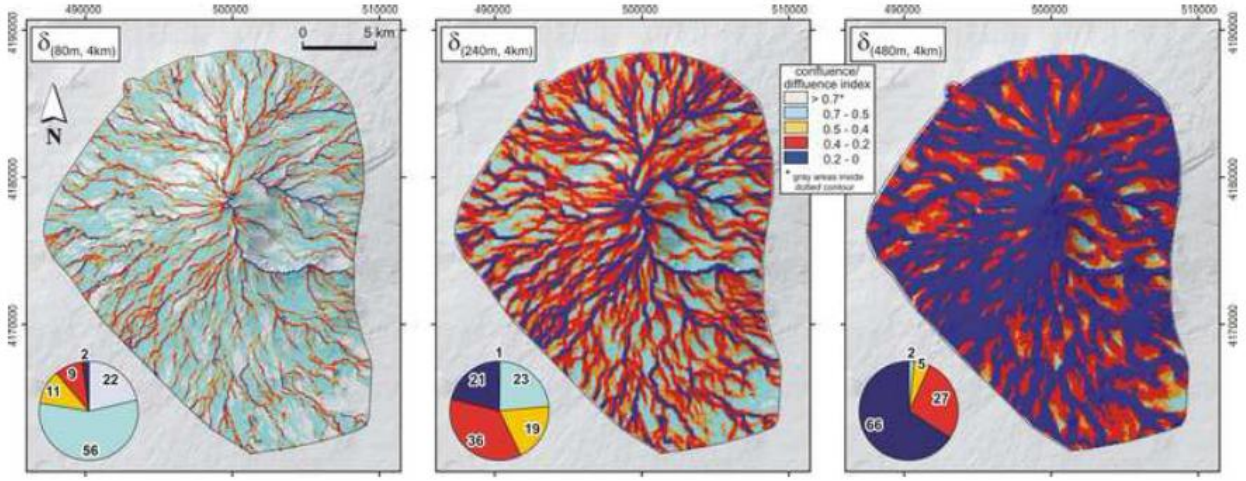

Figure 7

ACCEPTED MA

ACCEPTED MANUSCRIPT

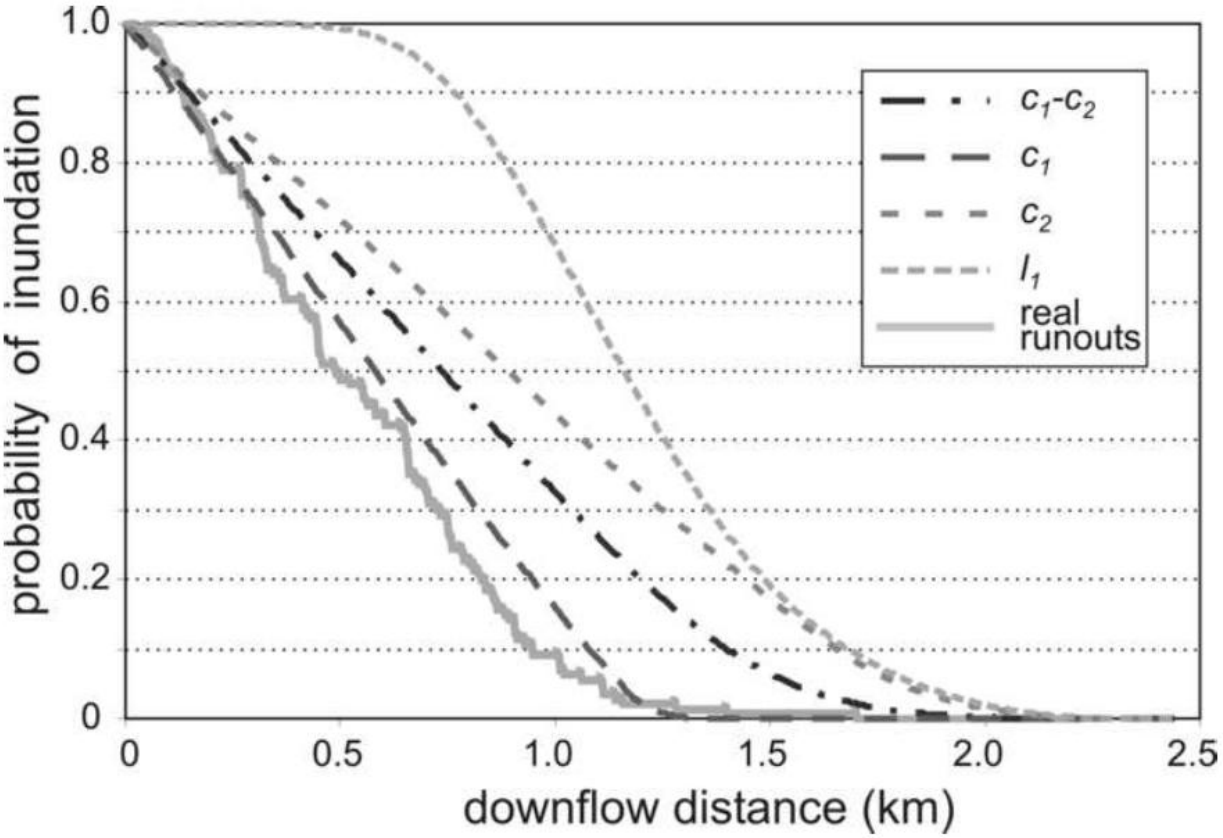

Figure 8

ACCEPTED

ACCEPTED MANUSCRIPT

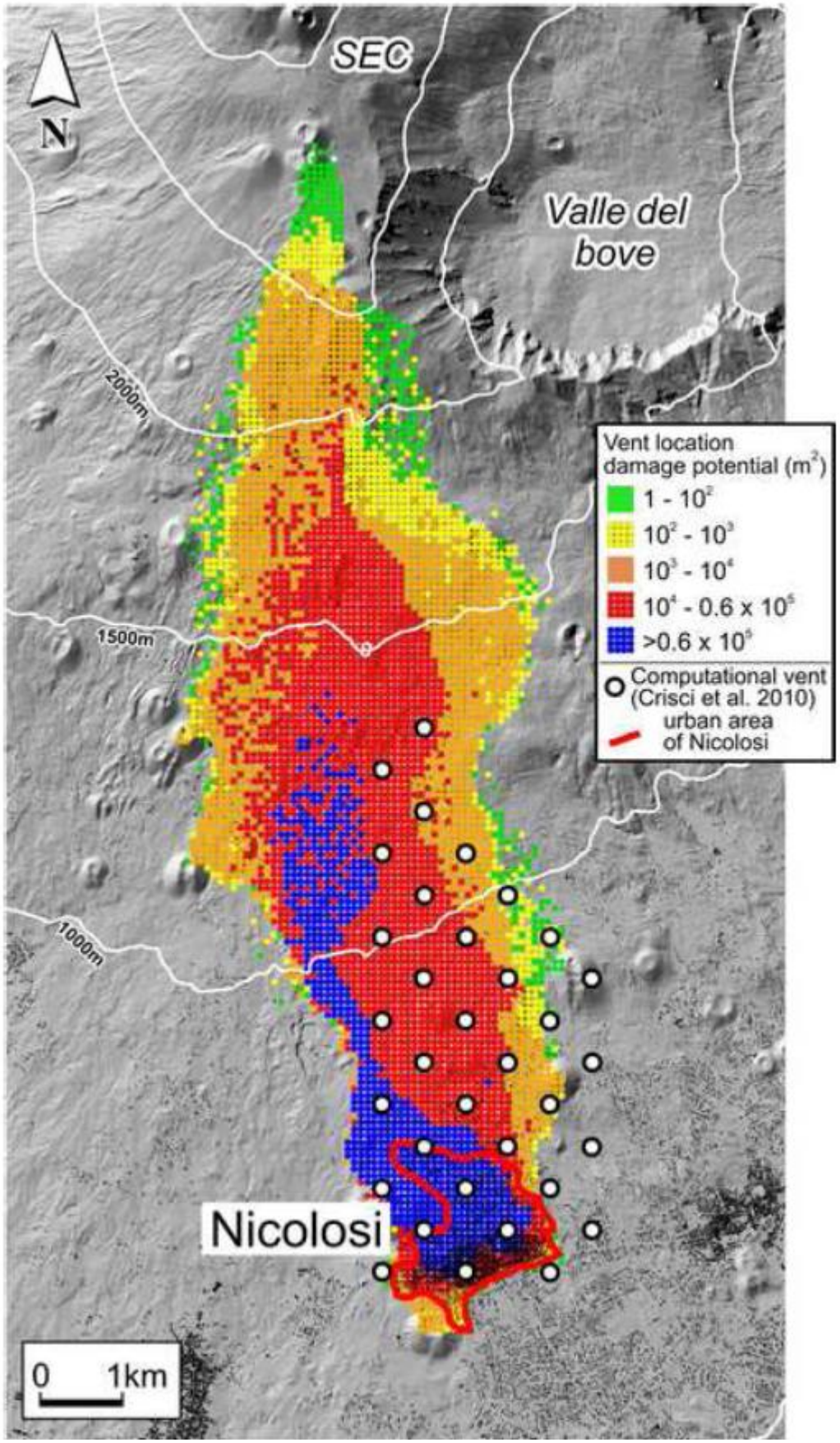

Figure 9

ACCEPTED MANUSCRIPT

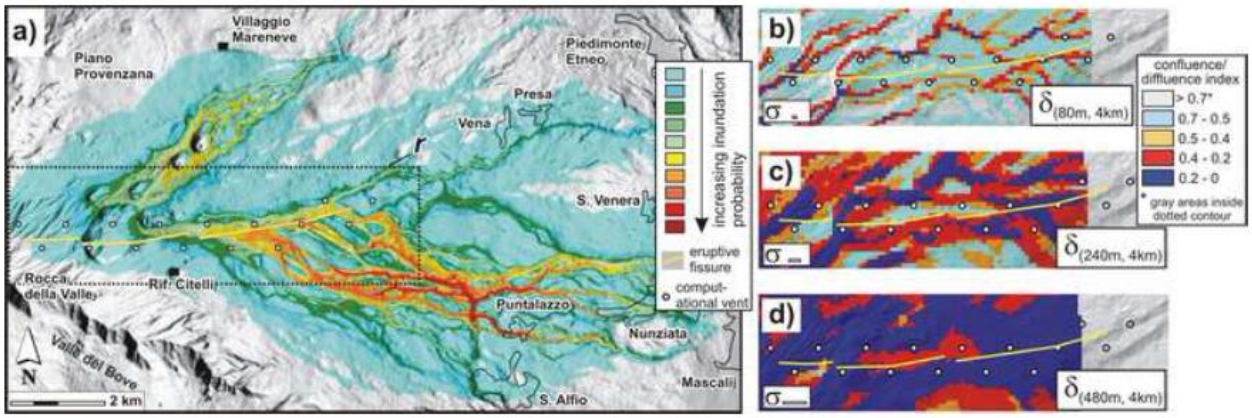

Figure 10

ACCEPTED MANUSCRIPT

ACCEPTED MANUSCRIPT

Highlights

Different input settings modify the hazard map of lava flows for Mount Etna;
the expected length of future lava flows results to be the critical parameter;
the effect of an error in vent position is quantified locally by a new index;

ACCEPTED MANUSCRIPT